

Background resilient quantitative phase microscopy using entangled photons

Yingwen Zhang,^{1,2,3,*} Paul-Antoine Moreau,^{4,5,†} Duncan England,² Ebrahim Karimi,^{1,2,3} and Benjamin Sussman^{2,1,3}

¹*Nexus for Quantum Technologies, University of Ottawa, Ottawa ON Canada, K1N6N5*

²*National Research Council of Canada, 100 Sussex Drive, Ottawa ON Canada, K1A0R6*

³*Joint Centre for Extreme Photonics, National Research Council and University of Ottawa, Ottawa, Ontario, Canada*

⁴*Department of Physics, National Cheng Kung University, Tainan, 70101, Taiwan*

⁵*Center for Quantum Frontiers of Research and Technology, NCKU, Tainan, 70101, Taiwan*

In this work, we introduce a quantum-based quantitative phase microscopy technique using a phase gradient approach that is inherently background resistant and does not rely on interferometry or scanning. Here, a transparent sample is illuminated by both photons of a position-momentum entangled pair with one photon setup for position measurement in the near-field (NF) of the sample and its partner for momentum measurement in the far-field (FF). By virtue of the spatial correlation property inherent to the entanglement, both the position and momentum information of the photons can thus be obtained simultaneously. The phase profile of the sample is then deduced through a phase gradient measurement obtained by measuring the centroid shift of the photons' in the FF momentum plane for each NF position. We show that the technique, while achieving an imaging resolution of $2.76\ \mu\text{m}$, is phase accurate to at least $\lambda/30$ and phase sensitive to $\lambda/100$ at a wavelength of 810 nm. In addition, through the temporal correlation between the photon pairs, our technique shows resilience to strong dynamic background lights, which can prove difficult to account for in classical phase imaging techniques. We believe this work marks a significant advancement in the capabilities of quantum phase microscopy and quantum imaging in general, it showcases imaging and phase resolutions approaching those attainable with classical phase microscopes. This advancement brings quantum imaging closer to practical real-world applications, heralding new possibilities in the field.

I. INTRODUCTION

Utilizing the properties of quantum entangled photons for sensing and imaging applications has been an active area of research in recent decades [1–5]. Quantum light offers a range of potential advantages over its classical counterpart in these applications, this includes super-resolution [6–10], robustness against noise [11–15], and additional functionalities such as immunity to dispersion [16, 17], hyperspectral imaging [18] and 3D imaging [19–21].

The use of entangled photons has also been extended to phase imaging. Phase imaging plays a pivotal role in revealing with enhanced clarity, the subtle variations in the optical path length of light passing through a transparent sample and has found widespread usage in biomedical science [22–24]. Interferometry based quantum phase retrieval techniques includes the use of photonic N00N states [25, 26] and the interference between successive laser passes of spontaneous parametric down-conversion (SPDC) events [27]. Phase imaging has also been demonstrated through holography with entangled photons [28, 29]. Non-interference methods includes ghost imaging approaches [30], the use of transport of intensity equation between intensity images obtained from different image planes [31, 32] and through the simultaneous measurement of the position and momentum information of photons through a Fourier Ptychography approach [33] and differential phase gradient approach [34]. These techniques offers various advantages such as sub-shot-noise sensitivity [25, 26, 31, 32], strong background-noise tolerance [28, 33] and ease of use, such as phase stability [29] or allowing scanning-free measurement compared to the classical counterpart [34].

In this study, we introduce a proof-of-concept demonstration showcasing a quantum-based quantitative phase microscopy technique using a phase gradient approach utilizing position-momentum entangled photons. The technique is shown to be resilient to the influence of background light and it does not rely on interferometry or scanning making it phase stable and requires no moving parts. As a property of position-momentum entanglement, a photon pair is correlated in position and anti-correlated in momentum, thus by measuring the position/momentum of one photon, one can deduce the position/momentum of the partner photon through the correlation property. By having both photons jointly illuminate a phase target then capturing one photon in the near-field (NF) plane of the target, which contains the photon's position information, and capturing the partner in the far-field (FF) plane, which contains the photon's momentum information, both the position and momentum of the photon pairs can be acquired simultaneously. Next,

* yzhang6@uottawa.ca

† pa.moreau@gs.ncku.edu.tw

using the relationship linking the phase gradient at a NF position with a corresponding centroid shift of the photons' location in the FF, we can quantitatively recover the phase profile of the target. This initial demonstration showcases an imaging resolution of $2.76\ \mu\text{m}$ or 362 line pairs per mm while being phase accurate to at least $\lambda/30$ and phase sensitive to $\lambda/100$ at a wavelength of 810 nm. In addition, through utilizing the temporal correlation between the entangled photons, we also demonstrate the technique's resilience against a strong dynamic background that fluctuates with space and time. This type of background can be especially challenging to correct for in classical phase imaging techniques.

Compared to earlier works exploiting position-momentum entangled photon pairs for phase measurement [33, 34], here, a different technique is used to extract the phase with significant improvements in both sensitivity and accuracy. This has allowed us to achieve imaging and phase resolutions close to that of classical phase microscopes demonstrating that our technique could readily be used for real world microscopy applications that requires low light levels or working under complex background lighting conditions. This is exemplified by the acquisition of the phase and amplitude images of biological cells.

II. EXPERIMENTAL SETUP

The setup of our quantum phase microscope is depicted in Fig. 1. A 20 mW, 405 nm continuous-wave (CW) laser, with a 1 mm beam diameter, is used to pump a 1 mm thick Type II periodically-poled potassium titanyl phosphate (ppKTP) crystal to generate, through the process of spontaneous parametric down-conversion (SPDC), orthogonally polarized photon pairs at 810 nm that are correlated in time and entangled in the position-momentum degrees of freedom. The photon pairs are directed through a 4f-imaging system to illuminate a phase target placed in the NF plane of the nonlinear crystal. The photons are then separated using a polarizing beamsplitter. The NF of the phase target is imaged onto a time-tagging camera (TPX3CAM [35, 36]) through the signal photons, while the FF of the target is projected onto a corner of the camera through a separate path using the idler photons. To identify photon pairs, time correlation measurement is conducted with a coincidence window of 20 ns. Because the photons are position-momentum entangled, we can infer the momentum of each signal photon detected at a NF position from the partnered idler photon, whose momentum is measured in the FF. Thus, 5-dimensional information, in time, position and momentum, is obtained for each photon.

To extract the phase information from a target that introduces a phase $\phi(x, y)$ to the photons, we determine the photons' mean propagation direction, given by the phase gradient $\vec{\theta}(x, y) = \vec{\nabla}[\phi(x, y) + \phi_0(x, y)]$, where $\phi_0(x, y)$ represents the photons' initial phase profile. Through a lens, this directional angle $\vec{\theta}(x, y)$ is directly measured as a position $\vec{k}(x, y) \approx f\vec{\theta}(x, y)$ in the FF (under the paraxial approximation), with f representing the lens focal length.

After detecting numerous photon pairs, we calculate the centroid position in each direction of $\vec{k} = u\hat{u} + v\hat{v}$ for all idler photons detected in the FF that are time-correlated with signal photons detected at position (x, y) in the NF. That is

$$\begin{aligned}\mathcal{U}(x, y) &= \frac{1}{N(x, y)} \sum_{n=1}^{N(x, y)} u_n(x, y) \\ \mathcal{V}(x, y) &= \frac{1}{N(x, y)} \sum_{n=1}^{N(x, y)} v_n(x, y),\end{aligned}\quad (1)$$

where $\mathcal{U}(x, y)$ and $\mathcal{V}(x, y)$ represent the centroid positions in the \hat{u} and \hat{v} directions for all idler photons temporally correlated with signal photons at position (x, y) in the NF, and $N(x, y)$ is the number of photon pairs detected at position (x, y) in the NF.

The expectation value of the phase gradient $\vec{\nabla}\phi(x, y)$ is then

$$\begin{pmatrix} \langle \frac{\partial\phi(x, y)}{\partial x} \rangle \\ \langle \frac{\partial\phi(x, y)}{\partial y} \rangle \end{pmatrix} = \frac{1}{f} \begin{pmatrix} \mathcal{U}(x, y) - \mathcal{U}_0(x, y) \\ \mathcal{V}(x, y) - \mathcal{V}_0(x, y) \end{pmatrix}, \quad (2)$$

with $\mathcal{U}_0(x, y)$ and $\mathcal{V}_0(x, y)$ representing the reference centroid positions obtained without the phase target.

Finally, the phase $\phi(x, y)$ is reconstructed by solving the two-dimensional partial differential equations $\frac{\partial\phi(x, y)}{\partial x}$ and $\frac{\partial\phi(x, y)}{\partial y}$. For this we use the Frankot and Chellappa method [37, 38]

$$\phi(x, y) = \mathcal{F}^{-1} \left[\frac{u\mathcal{F} \left[\frac{\partial\phi(x, y)}{\partial x} \right] + v\mathcal{F} \left[\frac{\partial\phi(x, y)}{\partial y} \right]}{i(u^2 + v^2)} \right], \quad (3)$$

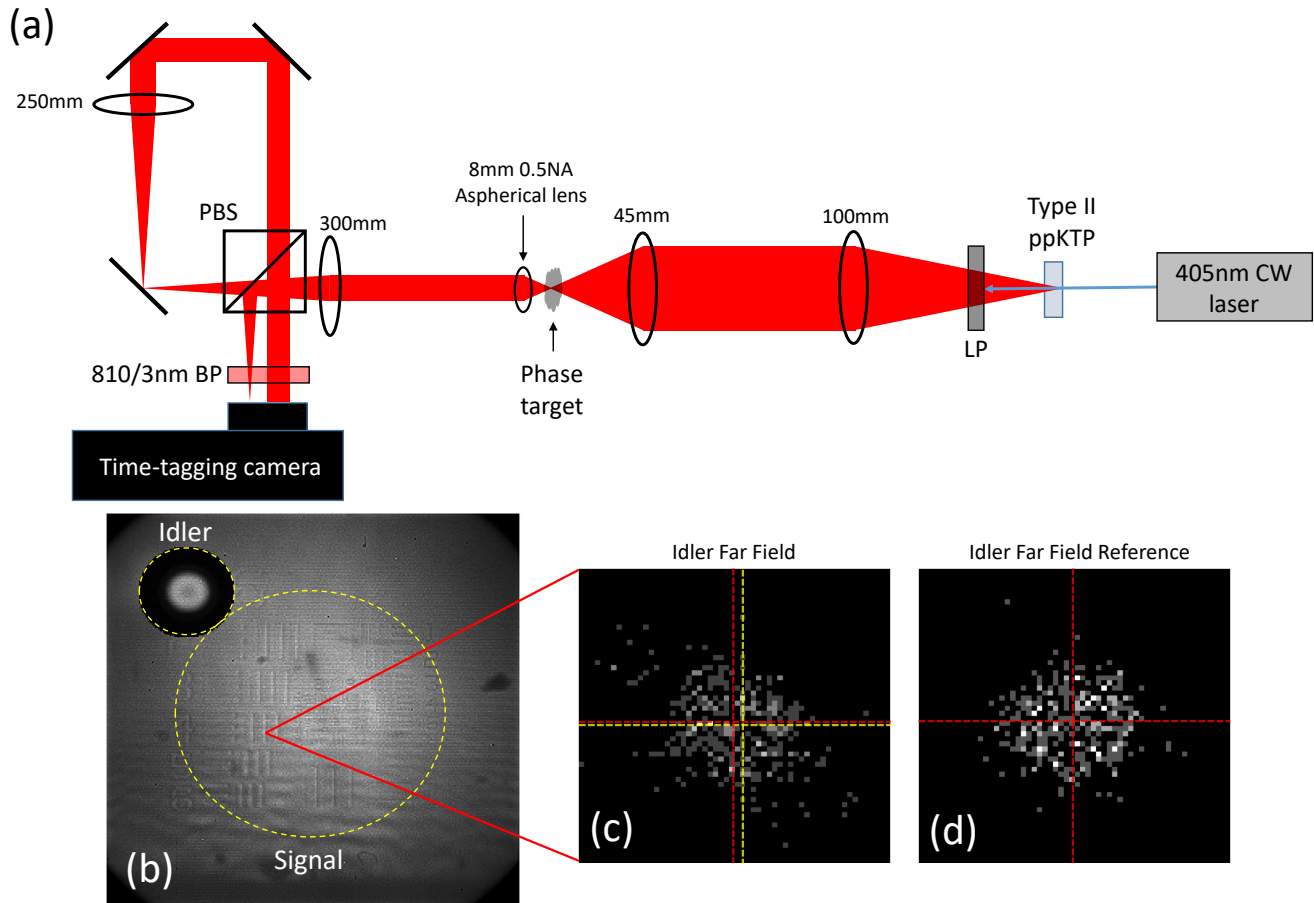


FIG. 1. **Experimental setup of quantum phase microscope** (a) Spatially entangled photon pairs with orthogonal polarization are generated through a Type II ppKTP crystal. After illuminating the target, the photon pairs are separated with a PBS such that the NF and FF of the target can be imaged separately by the signal and idler photons respectively. PBS: polarizing beamsplitter, LP filter: longpass filter, BP filter: bandpass filter, ppKTP: periodically-poled potassium titanyl phosphate crystal. (b) Brightfield image of a phase target with 200 nm feature height captured by the time-tagging camera. A time correlation measurement to identify photon pairs is then performed between all photons captured within the two highlighted circular regions. For viewing clarity, the idler beam shown here is scaled to be 50 times dimmer than measured to allow the signal beam to be visible in the same image. (c) Image formed by all idler photons in the FF that are detected in coincidence with signal photons that passed through the indicated NF pixel. (d) A reference idler photon image captured for the same NF pixel with no phase target in place. A centroid measurement is performed on each FF image for all NF pixels. Here the centroid for (c), indicated by the yellow crosshair, is shown relative to the centroid of the reference (d), indicated by the red crosshair.

where $\mathcal{F}[\cdot]$ and $\mathcal{F}^{-1}[\cdot]$ represent the Fourier and inverse Fourier transform, respectively. A derivation of this relation can be found in the Supplementary.

Before conducting these measurements with the phase target, a one-time reference measurement without the phase target in place is performed to determine $\phi_0(x, y)$. Note that background contributions has not been taken into account in eq. 1, see the Supplementary on the modifications required for background correction.

III. EXPERIMENTAL RESULTS

A. Quantitative phase measurement

To calibrate the accuracy of the phase recovery process we used quantitative phase targets (from Benchmark technologies [39]) with feature heights ranging from 50 nm to 350 nm, with two different patterns, the star and 1951 USAF. Measuring the average peak-to-peak phase difference in the patterns, we find the method is accurate from a

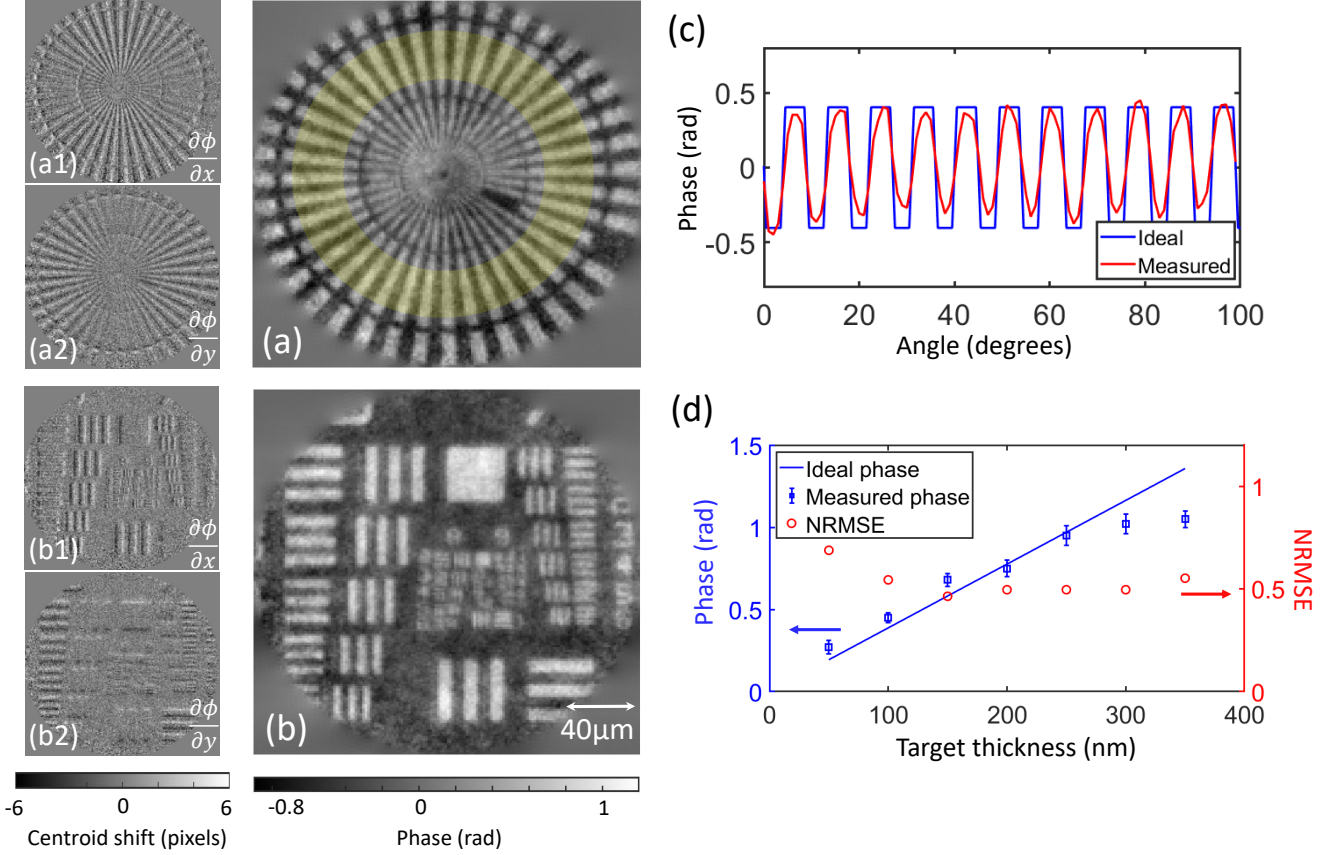


FIG. 2. **Results from imaging resolution phase targets** (a, b) Recovered phase images for a Star (a) and 1951 USAF (b) resolution phase target with 200 nm feature height. The corresponding measured phase gradient in the horizontal and vertical direction used to recover the phase image are shown in (a1, b1) and (a2, b2) respectively. (c) Cross-section from, 0 to 100 degrees, of the yellow highlighted regions of (a) compared to an ideal phase measurement of this target. (d) Measured phase (blue square) and NRMSE (red circle) as a function of the target thickness for the Star target. The phase is measured as the mean difference between the maxima and minima in the cross-section of the yellow highlighted regions as indicated in (a) and NRMSE compares the similarity between the measured phase profile to that of the ideal profile as shown in (c). The bright field image of the Star phase target can be seen in Fig. 4 and the full cross-sections can be found in the Supplementary. The measured phase of the USAF target can also be found in the Supplementary. Data acquisition time for all images shown in this and subsequent figures is 500 s. Background contributions has been corrected for in all results shown.

target thickness of 50 nm, or $\sim \lambda/30$ at 810 nm (the phase difference between 50 nm of glass and air) up to 200 nm, or $\lambda/8$. The smallest spatial feature observed in the microscope is group 8-4 of the 1951 USAF target, which corresponds to resolving line pairs separated by $2.76 \mu\text{m}$. The results for this are shown in Fig. 2. Based on the uncertainties in the phase measurement of approximately 0.06 rad, we would expect the technique to still be phase sensitive at approximately $\lambda/100$. The uncertainties in the phase measurement can be reduced with a longer data acquisition time or with a higher efficiency camera which will allow for even better phase accuracy and sensitivity, a more detailed discussion on this is given in the Discussions section. Note that we are not yet imaging at the diffraction limit of the imaging system, which given the numerical aperture of the lens arrangement is expected to be $\sim 1 \mu\text{m}$. This is a result of the large pixel size of the camera ($55 \mu\text{m}$) limiting the achievable resolution.

As a measure of the similarity between the recovered phase profile and that of an ideal phase profile, which has a constant phase across the target features, we determine the normalized root mean squared error (NRMSE) between the two phase profiles which is defined as

$$\text{NRMSE} = \frac{\sqrt{\frac{1}{N} \sum_{i=1}^N (O_i - E_i)^2}}{\bar{E}}, \quad (4)$$

where O_i and E_i are the observed and expected values, respectively. \bar{E} is the mean of the expected values. For better statistics we determined the NRMSE only for the cross-section of the star target. The NRMSE for the Star targets

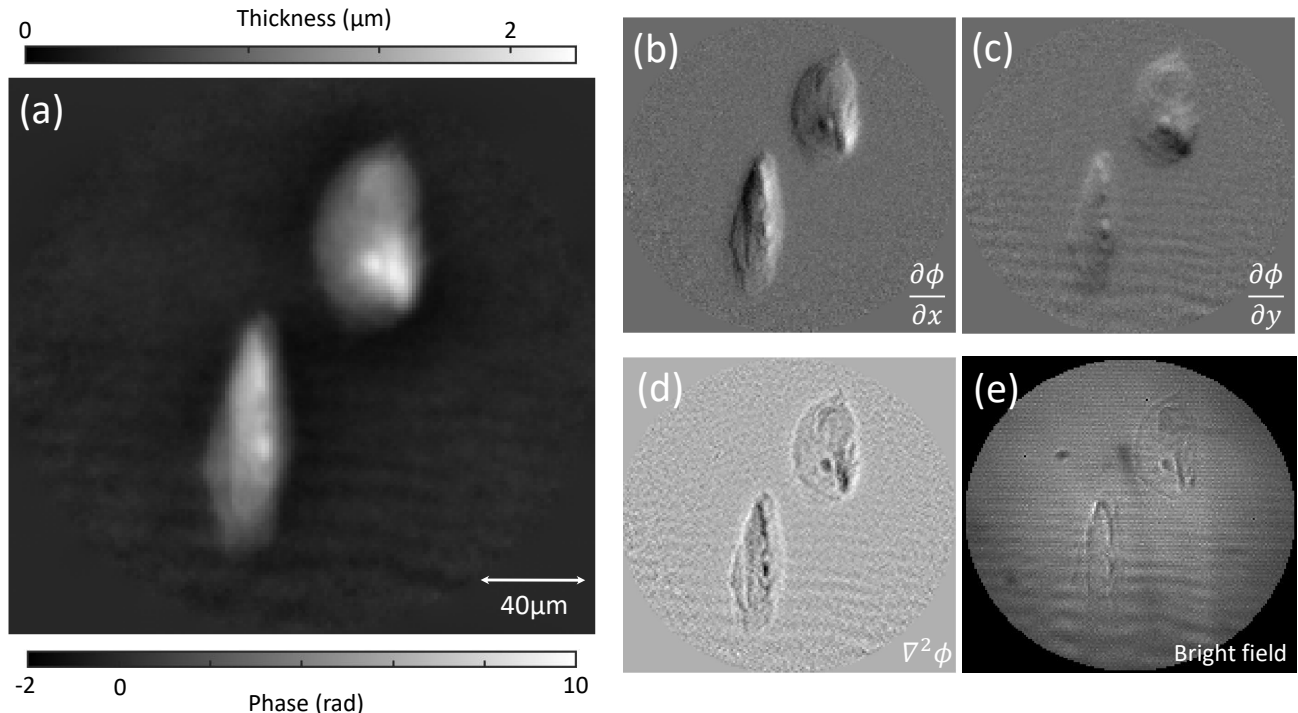


FIG. 3. **Results of imaging cheek epithelial cells** (a) Phase image of cheek epithelial cells. (b, c) The measured phase gradient in the horizontal and vertical direction for recovering the phase image (a). (d) The Laplacian of the phase. (e) Image of the cells captured directly by the camera as if through a conventional bright-field microscope.

of different heights are shown as red circles in Fig. 2(d).

From the results, we see that the NRMSE deteriorates for both smaller and larger feature heights. This outcome aligns with expectations. Smaller feature heights amplify the influence of background noise in relation to the subtle phase profile. For larger feature heights, the discrepancies between the measured and ideal phase profile can be due to a number of reasons. One is that the large phase jump will cause a very large phase gradient that diffracts photons to outside the numerical aperture of the FF imaging system, resulting in measuring a smaller centroid shift. The other being the linear relationship between the phase gradient and the FF centroid shift no longer holds for larger diffraction angles, due to the paraxial approximation being no longer valid. Therefore, the method is most accurate for targets that does not contain phase jumps of over 250 nm. It should be noted here that our analysis did not account for manufacturing irregularities in the quantitative phase targets which may exhibit deviations of up to 10% from the specified values, as stipulated by the manufacturer.

Lastly, in Fig. 3 we show the phase imaging of cheek epithelial cells where a refractive index of 1.35 [40] was assumed for the cells for estimating the thickness. We note that the Laplacian of the phase image, Fig. 3(d), can also be used to display features in the cells with a much better contrast as compared to the brightfield image as seen in Fig. 3(e).

B. Background mitigation

Quantitative phase imaging techniques are highly susceptible to the influence of background light. Addressing the background typically involves either separately measuring the background light or applying Fourier filtering techniques, which require some prior knowledge of the background characteristics. These methods are often limited in their effectiveness, especially against a dynamic backgrounds which fluctuates with space and time.

Here, we simulate the effect of a dynamic background by introducing numerically generated photon detection events from a Gaussian shaped beam profile into the raw camera data, both in the NF and FF. The properties of this background, including its intensity, width, and position, were all randomized over time. Refer to the Supplementary for more details on the background generation.

We demonstrate that, regardless of the background type, our approach of utilizing SPDC photons offers a robust

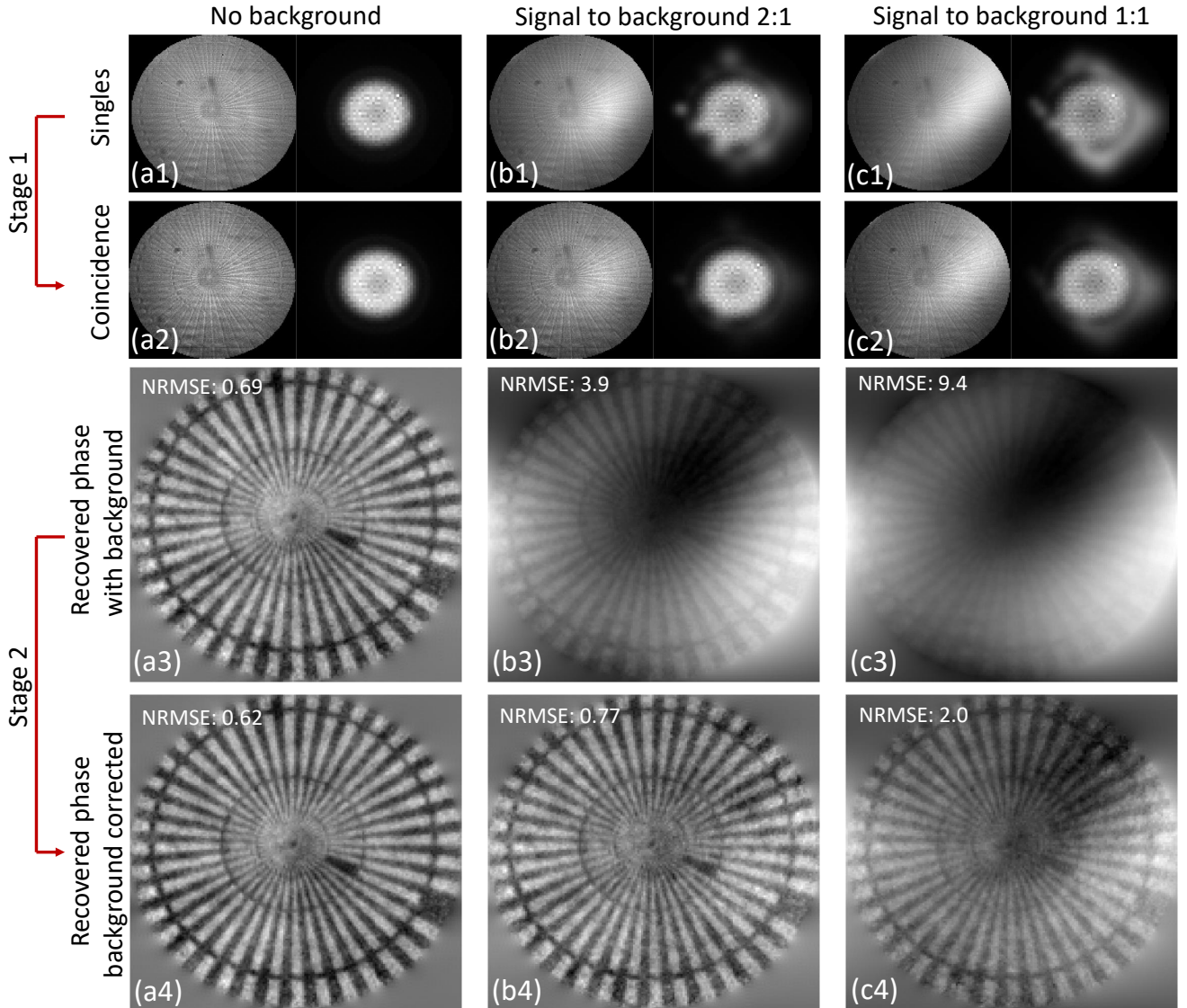


FIG. 4. **Results demonstrating background mitigation** (a1, b1, c1) NF and FF images obtained through direct imaging of the phase target with 200 nm feature heights when (a1) no background light is applied, (b1) a dynamic background light with approximately half the number of photons as compared to SPDC is added and (c1) when the dynamic background has approximately equal amount of photons as SPDC. (a2, b2, c2) NF and FF images after a time correlation measurement has been made to identify the photon pairs. It can be seen that a substantial amount of background light has been removed. (a3, b3, c3) Recovered phase image without applying background correction. (a4, b4, c4) Recovered phase images after background correction. The cross-section for all phase images can be found in the supplementary materials.

two-stage process to mitigate the impact of background light. The first stage relies on the coincident detection of photon pairs, this intrinsically provides background suppression as only photons arriving in the correct temporal window are included in the coincidence image. This type of background suppression, common to many imaging schemes based on entangled pairs [15, 41], is visually apparent when comparing Fig. 4(b1,c1) and (b2,c2).

However, even after coincidence detection, an uncorrelated background remains due to photons that accidentally arrive within the coincidence window despite not being generated in the same SPDC event. These are due to accidental coincidences between a SPDC photon and a background photon, two background photons, or two SPDC photons belonging to different pair events. In the second stage, the rate of accidental coincidences are measured by selecting a coincidence window that is outside of the true coincidence window, in this case, 50 ns before it. The contribution of background coincidences can then be subtracted from the the centroid shift to mitigate the effect of a dynamic background on the recovered phase profile. Refer to the Supplementary for more details on the detection

and subtraction of background light.

For weak background light, the dominant contribution in the background coincidences originates from the coincidences between different SPDC pairs generated within the coincidence window in which no spatial entanglement exists. Thus, the resultant background idler images will show no centroid shift. Consequently, the phase image in cases where this term is not subtracted will closely resemble the background-corrected phase image, albeit with a slightly smaller measured phase, as shown in Fig. 4(a). In Fig. 4(a3), for the star pattern having 200 nm feature heights and an expected phase of 0.81, the average measured phase without background-correction is 0.56 ± 0.04 , whereas in the background-corrected image, as seen in Fig. 4(a4), the measured phase is 0.74 ± 0.06 . The NRMSE is 0.62 for the background-corrected image and 0.69 for the uncorrected image. The difference can be seen more clearly in the cross-section of the phase target shown in the Supplementary.

In contrast, for strong backgrounds, a centroid shift will be introduced in the background idler image whenever the background light does not fall in the center of the detection area of the FF. This can be observed in Fig. 4(b3, c3) where strong distortions are seen in the recovered phase image. After background correction, our technique is able to recover the phase image with relatively good accuracy with a measured phase of 0.73 ± 0.08 and a NRMSE of 0.77 for (b4), where the total background photons is approximately half the number of SPDC photons. For Fig. 4(c4), where the total background photons is approximately equal to the number of SPDC photons, a phase of 0.68 ± 0.12 and a NRMSE of 2.0 is obtained.

C. Reduced far-field resolution

Since the phase recovery method is based on FF centroid shift, in principle, a high-resolution camera is not necessarily needed to perform the FF measurement. The centroid measurement can be performed with a resolution of just 2×2 pixels in the FF. Practically, this can be implemented by using a quadrant avalanche photodiode detector.

Here we demonstrate this in Fig. 5 by applying a 30×30 binning to the idler photon positions detected on the camera. i.e. $\lceil (u, v)/30 \rceil$ where (u, v) are the pixel position of the detected idler photon and $\lceil \cdot \rceil$ is the ceiling operation. The phase images obtained through 30×30 binning are quantitatively similar to those obtained at full resolution as seen in Fig. 2. However the reduced FF spatial resolution results in a larger uncertainty (by between 20% to 70% depending on the size of the phase jump), and increased NRMSE (by approximately 10% on average). With 2×2 pixel FF resolution, though less accurate in the phase measurement, as a result, becomes more tolerant to background influences. In Fig. 5(b), when a 30×30 binning is applied to the FF detector on the same dataset used in Fig.4(c), a much better background tolerance is observed. A NRSME of 1.0 is obtained in Fig. 5(b) compared to 2.0 for Fig.4(c4).

This demonstrates another versatility of our technique, in that it can be switched, all in post-processing, from having better phase accuracy to better background tolerance, depending on the requirement.

IV. DISCUSSION

In summary, by utilizing the inherent correlations of position-momentum entangled photons, we demonstrated a scanning-free, non-interferometric quantitative phase microscopy technique which is inherently resilient to the influence of background light. This approach allows for the simultaneous measurement of the position and momentum of photons diffracted from a phase target, facilitating the reconstruction of the target's phase profile via a phase gradient method. This initial demonstration achieved an imaging resolution of $2.76 \mu\text{m}$ or 362 line pairs per mm with the phase measurement tested to be accurate at $\lambda/30$ at a wavelength of 810 nm and is phase sensitive to $\lambda/100$. Additionally, through taking advantage of the temporal correlation between the photon pairs, we show that the phase image of a target can still be recovered with good accuracy under a strong, dynamic background. Lastly, our technique has the versatility to be switched, all in post-processing, from having better phase accuracy to better background tolerance by changing the effective FF resolution for momentum measurements. Though we demonstrated phase microscopy using this technique, it can also be used as a wavefront sensor for adaptive optics.

Our technique bears the closest classical resemblance to the Shack-Hartmann (SH) wavefront sensor [42]. The SH sensor employs a microlens array to capture both the position and momentum attributes of incident light rays, subsequently utilizing this data to deduce the phase information via phase gradient measurements. Though more commonly used in the field of adaptive optics [43], the SH sensor has also been demonstrated for use in quantitative phase microscopy [38]. Nevertheless, our quantum method offers numerous advantages beyond its robustness against background light. Most notably it obviates the need for microlens arrays, thereby mitigating several challenges inherent to SH sensors. Firstly, a SH sensor requires a total of $N_n \times N_f$ pixels, with N_n and N_f being the NF and FF pixel resolution respectively, while our quantum technique only requires $N_n + N_f$ pixels. Secondly, we circumvent the issue of cross-talk between pixels situated behind neighboring microlenses, a common problem encountered in

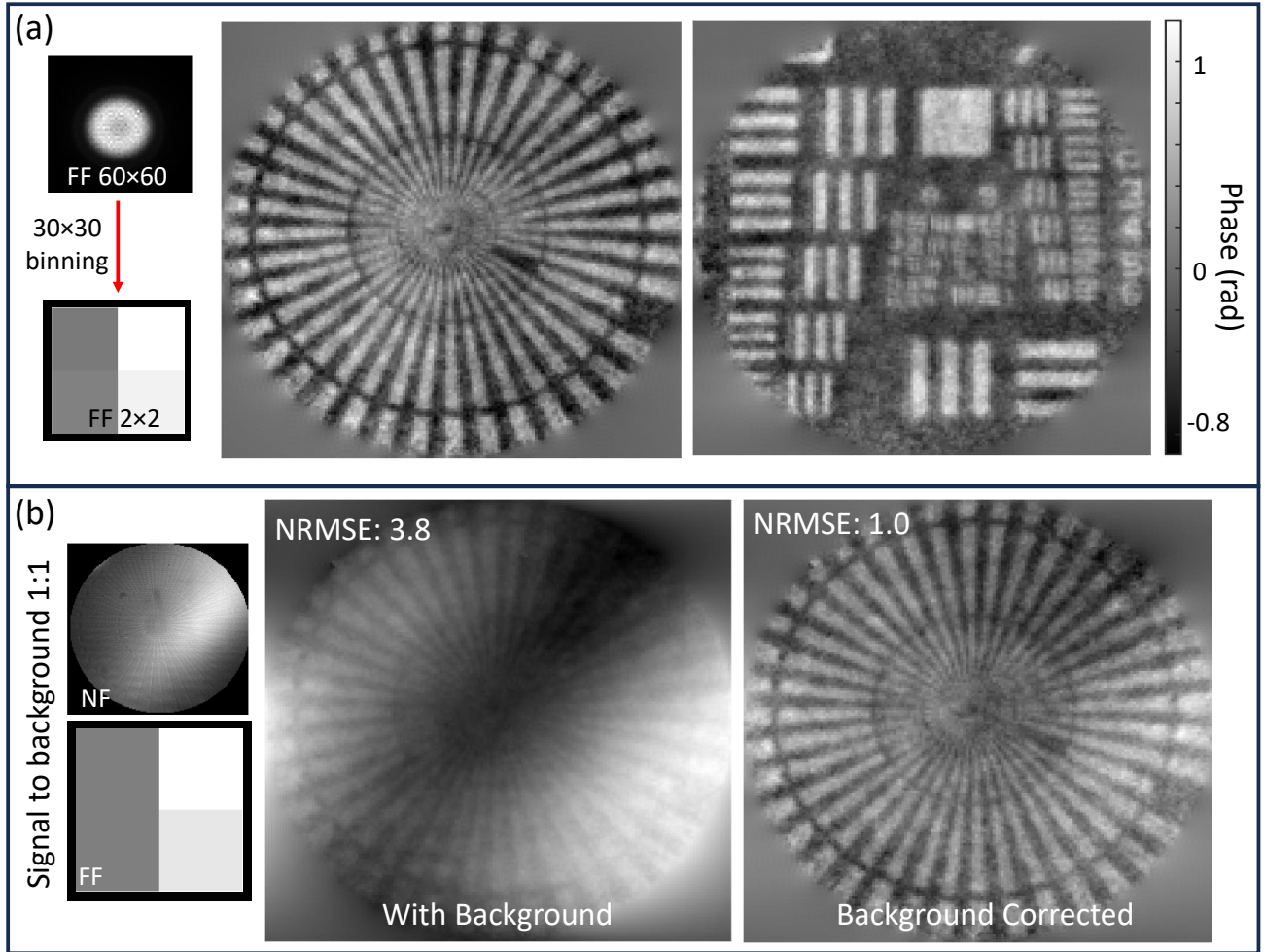


FIG. 5. **Results from 2×2 pixels FF resolution** (a) Recovered phase images for a Star and 1951 USAF resolution phase target with 200 nm feature heights using 2×2 pixels FF resolution. (b) Recovered phase images for a Star resolution phase target with 200 nm feature heights before and after background correction using 2×2 pixels FF resolution. The background to SPDC photon ratio is $\sim 1:1$. A full comparison with the results of Fig. 2 and 4 can be found in the Supplementary.

SH sensors when encountering large phase gradient, leading to overlapping FF beams beneath adjacent microlenses. Lastly, our technique employs standard 1- and 2-inch diameter lenses, which can be constructed with much higher quality compared to the less-ideal shape of microlens arrays and is less prone to misalignment, thus reducing the occurrence of aberrations [44, 45].

Other similar classical non-interferometric phase imaging techniques that involve imaging both the NF and FF includes Ptychography [46] and the Gerchberg-Saxton (GS) algorithm [47]. However, Ptychography requires scanning of the NF and the GS algorithm is not always convergent, our quantum technique does not have either of these two short comings.

The data acquisition speed of our technique is currently limited by the available camera technology. Our camera system exhibits a quantum efficiency of approximately 7%, an 8 ns time-resolution, and a maximum photon detection rate of approximately 10^7 photons per second, as detailed in [48]. A seven-fold improvement in each of the three camera parameters mentioned above could potentially reduce the required data acquisition time to a second. Such enhancements would not only expedite data collection but also significantly enhance the phase sensitivity and accuracy of the technique due to an increased coincidence rate. Considering the rapid advancements in single-photon detection technology witnessed in recent years, the prospect of developing time-tagging single-photon cameras meeting these specifications appears to be within reach in the near future.

During the submission of this work, we are made aware of a work using a similar phase gradient approach but using

a SH sensor instead of a time-tagging camera for the measurement of biphoton spatial wave function [49].

-
- [1] M. Genovese, *Journal of Optics* **18**, 073002 (2016).
- [2] I. R. Berchera and I. P. Degiovanni, *Metrologia* **56**, 024001 (2019).
- [3] P.-A. Moreau, E. Toninelli, T. Gregory, and M. J. Padgett, *Nature Reviews Physics* **1**, 367 (2019).
- [4] C. L. Degen, F. Reinhard, and P. Cappellaro, *Rev. Mod. Phys.* **89**, 035002 (2017).
- [5] S. Pirandola, B. R. Bardhan, T. Gehring, C. Weedbrook, and S. Lloyd, *Nature Photonics* **12**, 724 (2018).
- [6] M. Tsang, *Phys. Rev. Lett.* **102**, 253601 (2009).
- [7] H. Shin, K. W. C. Chan, H. J. Chang, and R. W. Boyd, *Phys. Rev. Lett.* **107**, 083603 (2011).
- [8] L. A. Rozema, J. D. Bateman, D. H. Mahler, R. Okamoto, A. Feizpour, A. Hayat, and A. M. Steinberg, *Phys. Rev. Lett.* **112**, 223602 (2014).
- [9] M. Unternährer, B. Bessire, L. Gasparini, M. Perenzoni, and A. Stefanov, *Optica* **5**, 1150 (2018).
- [10] R. Tenne, U. Rossman, B. Rephael, Y. Israel, A. Krupinski-Ptaszek, R. Lapkiewicz, Y. Silberberg, and D. Oron, *Nature Photonics* **13**, 116 (2019).
- [11] G. Brida, M. Genovese, and I. Ruo Berchera, *Nature Photonics* **4**, 227 (2010).
- [12] N. Samantaray, I. Ruo-Berchera, A. Meda, and M. Genovese, *Light: Science & Applications* **6**, e17005 (2017).
- [13] Y. Zhang, D. England, A. Nomerotski, P. Svihra, S. Ferrante, P. Hockett, and B. Sussman, *Phys. Rev. A* **101**, 053808 (2020).
- [14] H. Defienne, J. Zhao, E. Charbon, and D. Faccio, *Phys. Rev. A* **103**, 042608 (2021).
- [15] J. Zhao, A. Lyons, A. C. Ulku, H. Defienne, D. Faccio, and E. Charbon, *Opt. Express* **30**, 3675 (2022).
- [16] M. B. Nasr, B. E. A. Saleh, A. V. Sergienko, and M. C. Teich, *Phys. Rev. Lett.* **91**, 083601 (2003).
- [17] P. Yepiz-Graciano, Z. Ibarra-Borja, R. Ramírez Alarcón, G. Gutiérrez-Torres, H. Cruz-Ramírez, D. Lopez-Mago, and A. B. U'Ren, *Phys. Rev. Applied* **18**, 034060 (2022).
- [18] Y. Zhang, D. England, and B. Sussman, *Opt. Express* **31**, 2282 (2023).
- [19] B. Ndagano, H. Defienne, D. Branford, Y. D. Shah, A. Lyons, N. Westerberg, E. M. Gauger, and D. Faccio, *Nature Photonics* **16**, 384 (2022).
- [20] Y. Zhang, A. Orth, D. England, and B. Sussman, *Phys. Rev. A* **105**, L011701 (2022).
- [21] Y. Zhang, D. England, A. Orth, E. Karimi, and B. Sussman, *Phys. Rev. Appl.* **21**, 024029 (2024).
- [22] Y. Park, C. Depeursinge, and G. Popescu, *Nature Photonics* **12**, 578 (2018).
- [23] V. Micó, J. Zheng, J. Garcia, Z. Zalevsky, and P. Gao, *Adv. Opt. Photon.* **11**, 135 (2019).
- [24] T. L. Nguyen, S. Pradeep, R. L. Judson-Torres, J. Reed, M. A. Teitell, and T. A. Zangle, *ACS Nano* **16**, 11516 (2022), PMID: 35916417, <https://doi.org/10.1021/acsnano.1c11507>.
- [25] T. Ono, R. Okamoto, and S. Takeuchi, *Nature Communications* **4**, 2426 (2013).
- [26] Y. Israel, S. Rosen, and Y. Silberberg, *Phys. Rev. Lett.* **112**, 103604 (2014).
- [27] A. N. Black, L. D. Nguyen, B. Braverman, K. T. Crampton, J. E. Evans, and R. W. Boyd, *Optica* **10**, 952 (2023).
- [28] H. Defienne, B. Ndagano, A. Lyons, and D. Faccio, *Nature Physics* **17**, 591 (2021).
- [29] G. Thekkadath, D. England, F. Bouchard, Y. Zhang, M. Kim, and B. Sussman, *Science Advances* **9**, eadh1439 (2023), <https://www.science.org/doi/pdf/10.1126/sciadv.adh1439>.
- [30] A. F. Abouraddy, P. R. Stone, A. V. Sergienko, B. E. A. Saleh, and M. C. Teich, *Phys. Rev. Lett.* **93**, 213903 (2004).
- [31] C.-H. Lu, M. Reichert, X. Sun, and J. W. Fleischer, “Quantum phase imaging using spatial entanglement,” (2015), arXiv:1509.01227 [physics.optics].
- [32] G. Ortolano, A. Paniate, P. Boucher, C. Napoli, S. Soman, S. F. Pereira, I. Ruo-Berchera, and M. Genovese, *Light: Science & Applications* **12**, 171 (2023).
- [33] T. Aidukas, P. C. Konda, A. R. Harvey, M. J. Padgett, and P.-A. Moreau, *Scientific Reports* **9**, 10445 (2019).
- [34] H. Hodgson, Y. Zhang, D. England, and B. Sussman, *Applied Physics Letters* **122**, 034001 (2023), <https://doi.org/10.1063/5.0133980>.
- [35] A. Nomerotski, *Nuclear Instruments and Methods in Physics Research Section A: Accelerators, Spectrometers, Detectors and Associated Equipment* **937**, 26 (2019).
- [36] “<https://kt.cern/technologies/timepix3>,” .
- [37] R. Frankot and R. Chellappa, *IEEE Transactions on Pattern Analysis and Machine Intelligence* **10**, 439 (1988).
- [38] H. Gong, T. E. Agbana, P. Pozzi, O. Soloviev, M. Verhaegen, and G. Vdovin, *Opt. Lett.* **42**, 2122 (2017).
- [39] “<https://benchmarktech.com/quantitativephasemicroscop/>,” .
- [40] B. Gul, S. Ashraf, S. Khan, H. Nisar, and I. Ahmad, *Photodiagnosis and Photodynamic Therapy* **33**, 102096 (2021).
- [41] D. G. England, B. Balaji, and B. J. Sussman, *Phys. Rev. A* **99**, 023828 (2019).
- [42] R. V. Shack, *Spring Meeting of Optical Society of America*, 1971 **656** (1971).
- [43] R. Tyson and B. Frazier, *Principles of Adaptive Optics* (CRC Press, 2022).
- [44] J. Pfund, N. Lindlein, and J. Schwider, *Appl. Opt.* **37**, 22 (1998).
- [45] A. Chernyshov, U. Sterr, F. Riehle, J. Helmcke, and J. Pfund, *Appl. Opt.* **44**, 6419 (2005).
- [46] J. Rodenburg and A. Maiden, “Ptychography,” in *Springer Handbook of Microscopy*, edited by P. W. Hawkes and J. C. H. Spence (Springer International Publishing, Cham, 2019) pp. 819–904.

- [47] R. W. Gerchberg, *Optik* **35**, 237 (1972).
 [48] V. Vidyapin, Y. Zhang, D. England, and B. Sussman, *Scientific Reports* **13**, 1009 (2023).
 [49] Y. Zheng, Z.-D. Liu, R.-H. Miao, J.-M. Cui, M. Yang, X.-Y. Xu, J.-S. Xu, C.-F. Li, and G.-C. Guo, “Characterizing biphoton spatial wave function dynamics with quantum wavefront sensing,” (2024), arXiv:2406.04973 [quant-ph].

THE FRANKOT AND CHELLAPPA METHOD

Letting $p(x, y) = \frac{\partial \phi(x, y)}{\partial x}$ and $q(x, y) = \frac{\partial \phi(x, y)}{\partial y}$ be the measured phase gradients, the Laplacian for the phase $\phi(x, y)$ can be written as

$$\nabla^2 \phi(x, y) = \frac{\partial^2 \phi(x, y)}{\partial x^2} + \frac{\partial^2 \phi(x, y)}{\partial y^2} = \frac{\partial p(x, y)}{\partial x} + \frac{\partial q(x, y)}{\partial y}. \quad (5)$$

Given the Fourier transform and inverse Fourier transform defined as

$$\begin{aligned} \mathcal{F} [f(x, y)] &= \hat{f}(u, v) = \int \int f(x, y) e^{-i(ux+vy)} dx dy \\ \mathcal{F}^{-1} [\hat{f}(u, v)] &= f(x, y) = \frac{1}{2\pi} \int \int \hat{f}(u, v) e^{i(ux+vy)} du dv, \end{aligned} \quad (6)$$

and using the differentiation property of the Fourier transform

$$\mathcal{F} \left[\frac{d^n}{dx^n} f(x) \right] = (iu)^n \hat{f}(u), \quad (7)$$

we can write the Fourier transform of Eq. 5 as

$$\begin{aligned} \mathcal{F} \left[\frac{\partial^2 \phi(x, y)}{\partial x^2} + \frac{\partial^2 \phi(x, y)}{\partial y^2} \right] &= \mathcal{F} \left[\frac{\partial p(x, y)}{\partial x} + \frac{\partial q(x, y)}{\partial y} \right] \\ &= -(u^2 + v^2) \hat{\phi}(u, v) = iu \hat{p}(u, v) + iv \hat{q}(u, v). \end{aligned} \quad (8)$$

Thus, knowing the phase gradients $p(x, y)$ and $q(x, y)$ and computing their Fourier transforms $\hat{p}(u, v)$ and $\hat{q}(u, v)$, the phase $\phi(x, y)$ can be recovered through the inverse Fourier transform of Eq. 8

$$\phi(x, y) = \mathcal{F}^{-1} \left[\frac{u \hat{p}(u, v) + v \hat{q}(u, v)}{i(u^2 + v^2)} \right]. \quad (9)$$

BACKGROUND GENERATION, DETECTION AND SUBTRACTION

Background photon events are numerically generated and inserted into the raw camera data. A random number generator is used to generate the detected position and time for each photon from a background light with Gaussian beam profile exhibiting Poissonian photon number statistics. This background is applied to both the NF and FF. Parameters for the intensity, width, and location of the Gaussian shaped background is randomized every 25s to simulate a dynamic background. The background is chosen to be randomized every 25s and not at a much faster rate so as not to create an overall background that is uniform in intensity after the 500s data acquisition time. For the data in Fig. 4(b) of the main text, the background intensity in each image plane is on average $\sim 0.5 \times 10^6$ photons per second, and for Fig. 4(c) of the main text this is $\sim 1 \times 10^6$ photons per second. In comparison, the number of detected SPDC photons in each image plane is $\sim 1.1 \times 10^6$ photons per second. For better comparison, the same seed is used in the random number generation of the width and location for the background light at the two different intensity levels. An illustration on how the background is added to the NF and FF with time is shown in Fig. 6(a).

Figure 6(b) is a typical histogram showing the difference in arrival time between two photons detected in the two regions of the camera. The central peak is the result of time-correlated SPDC photon pairs being detected at the same time. On the other hand a constant background is also visible in the histogram, this is from the detection of coincidence between uncorrelated photons. It is not possible to determine which of the photon pairs detected are from background light, however, one can determine the resultant contribution of the background. To obtain the background contribution, the coincidence window is shifted away from the central peak. All photon pair events detected within this window will be from only uncorrelated photons. Since the background coincidence rate is uniform in time on the

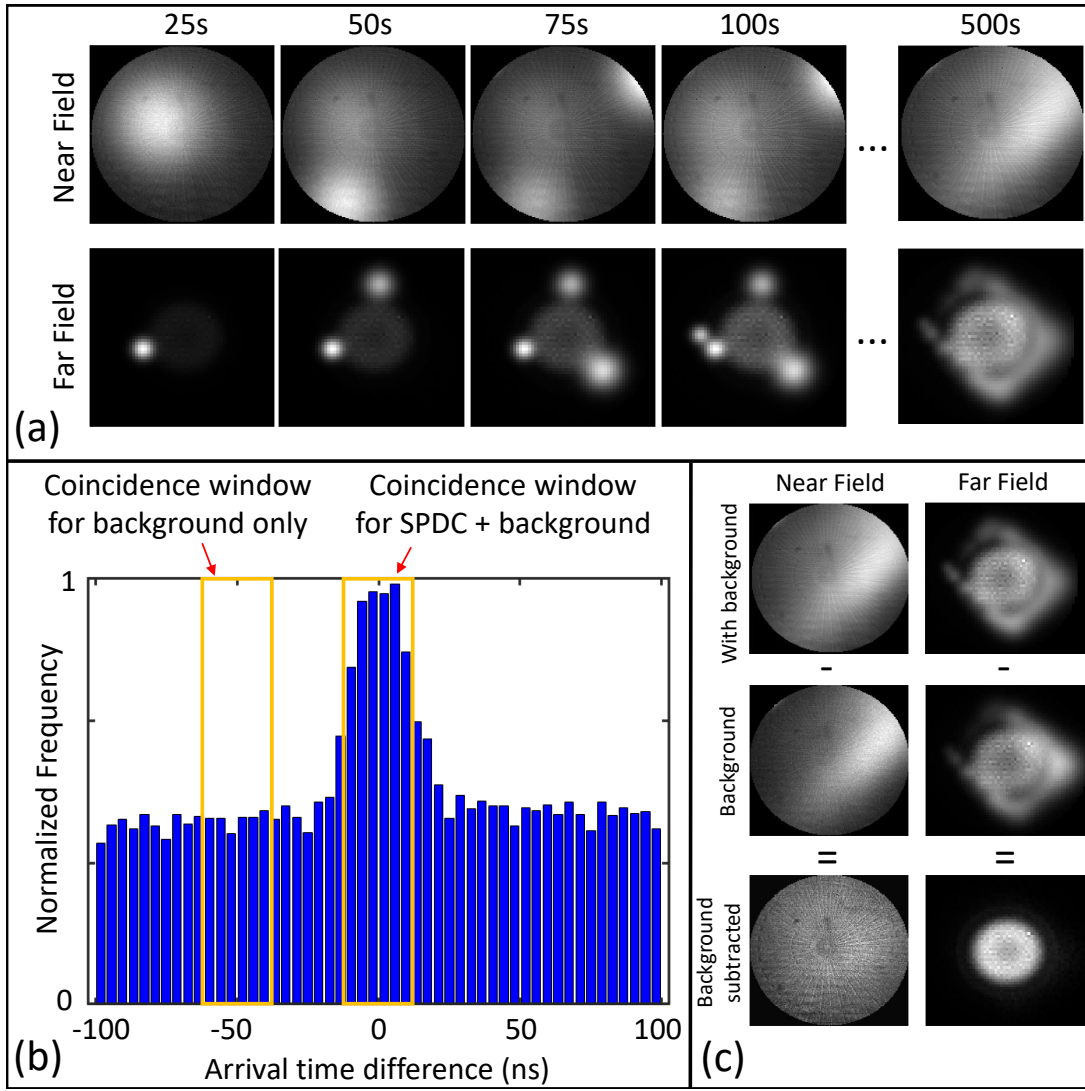


FIG. 6. **Background generation and detection** (a) Shows the numerically added background light to the NF and FF whose parameters are randomized every 25 s. (b) A typical coincidence histogram taken showing the number of events detected as a function of the difference in arrival time between the photons detected on the two regions of the camera. The location and width of the coincidence window for identifying all photons detected in coincidence and only that of background coincidences are highlighted in orange. (c) Verifying the validity of the background identification approach illustrated in (b) through subtracting the obtained background image from the image containing all coincidences.

nanosecond timescale, this measurement is representative of the accidental coincidence rate in the central window. It can be verified that the resultant image formed by the uncorrelated photon pairs is indeed the background by subtracting it directly from the coincidence image to obtain a background free image, as shown in Fig. 6(c).

Due to the timing resolution of the camera, a 50 ns shift in the coincidence window is used in this experiment. For a detector with better timing resolution, which will result in a narrower central peak for SPDC, a smaller shift can be used. Note that this method of background identification is only valid when the background fluctuation is slower than the applied shift to the coincidence window.

Now with the position information on each detected photon pair from the background correlation measurement,

the background contribution is subtracted from the centroid shift by modifying eq. 1 as follows:

$$\begin{aligned}\mathcal{U}(x, y) &= \frac{1}{N(x, y) - N_b(x, y)} \left(\sum_{n=1}^{N(x, y)} u_n(x, y) - \sum_{m=1}^{N_b(x, y)} u_m^b(x, y) \right) \\ \mathcal{V}(x, y) &= \frac{1}{N(x, y) - N_b(x, y)} \left(\sum_{n=1}^{N(x, y)} v_n(x, y) - \sum_{m=1}^{N_b(x, y)} v_m^b(x, y) \right),\end{aligned}\tag{10}$$

where $N_b(x, y)$ is the number of background coincidences detected at position (x, y) in the NF and $u^b(x, y)$ and $v^b(x, y)$ are the positions of the background photons detected in the FF, in coincidence with those detected at position (x, y) in the NF.

IMAGES OF FULL DATA SET

Figure 7 shows the recovered phase images and cross-sections for all Star resolution phase targets with full far-field (FF) resolution and 2×2 pixels FF resolution. Figure 8 shows the recovered phase and NRMSE as a function of the target thickness for the Star target as determined from Fig. 7. Figure 9 shows the recovered phase images and cross-sections for all 1951 USAF resolution phase targets with full FF resolution and 2×2 pixels FF resolution. Figure 10 shows the recovered phase as a function of the target thickness for the 1951 USAF target as determined from Fig. 9. Figure 11 shows the recovered phase images and cross-sections of the Star resolution phase targets used to illustrate background subtraction.

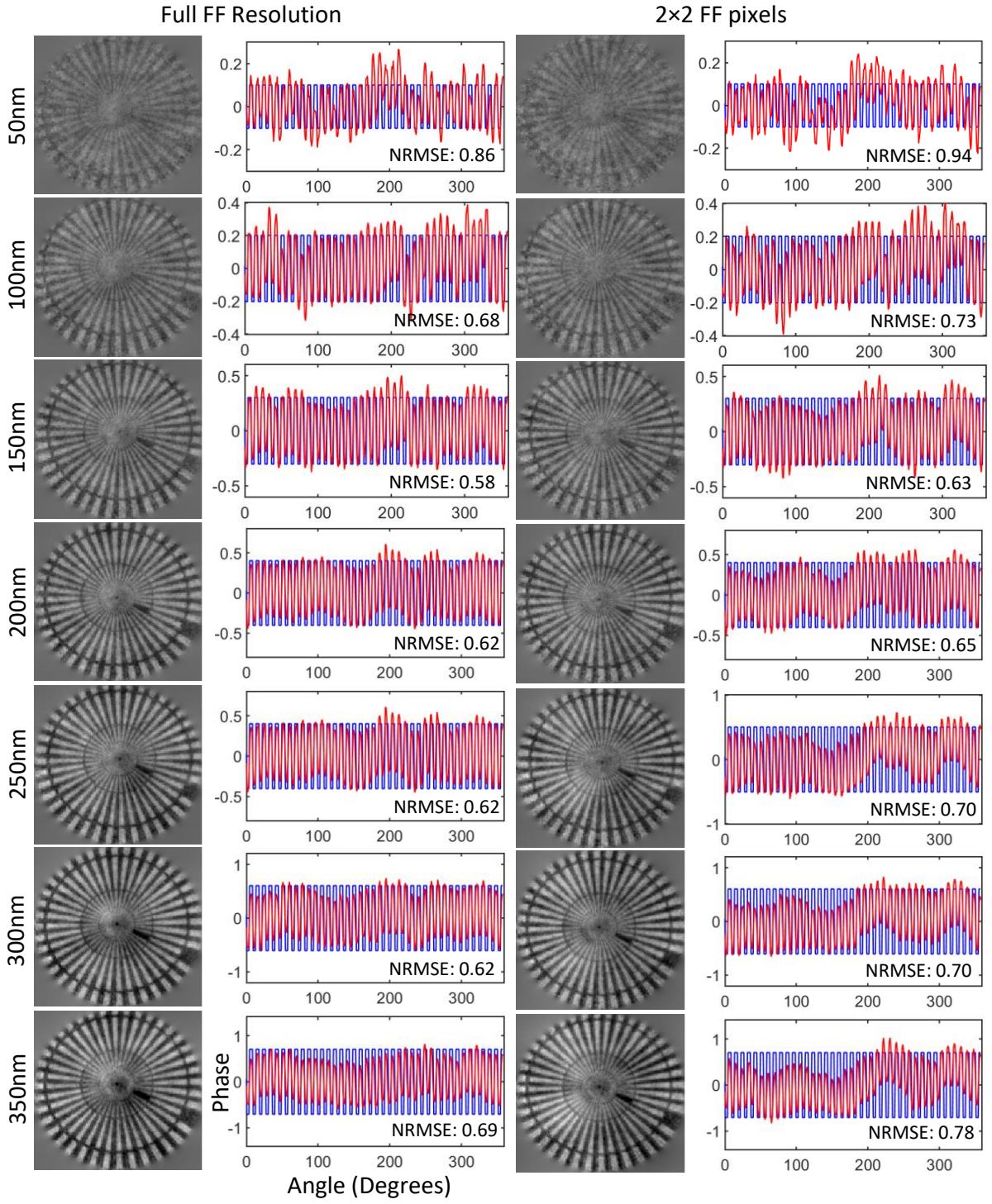


FIG. 7. Recovered phase image and cross-section of all Star resolution phase targets.

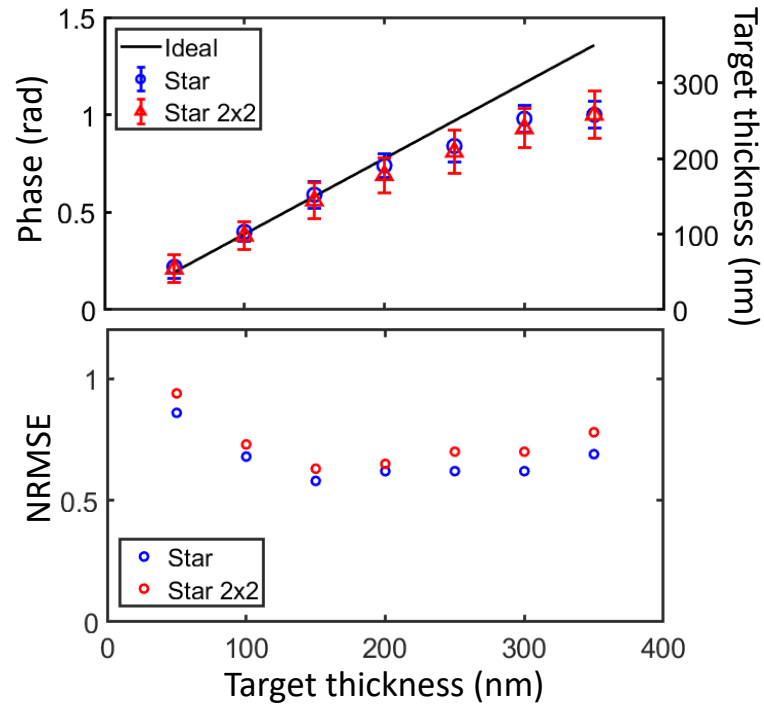


FIG. 8. Recovered phase and NRMSE as a function of the target thickness for the Star target. Red are the results for after a 30×30 binning is applied to the idler photons' position, whereas blue are when no binning is applied.

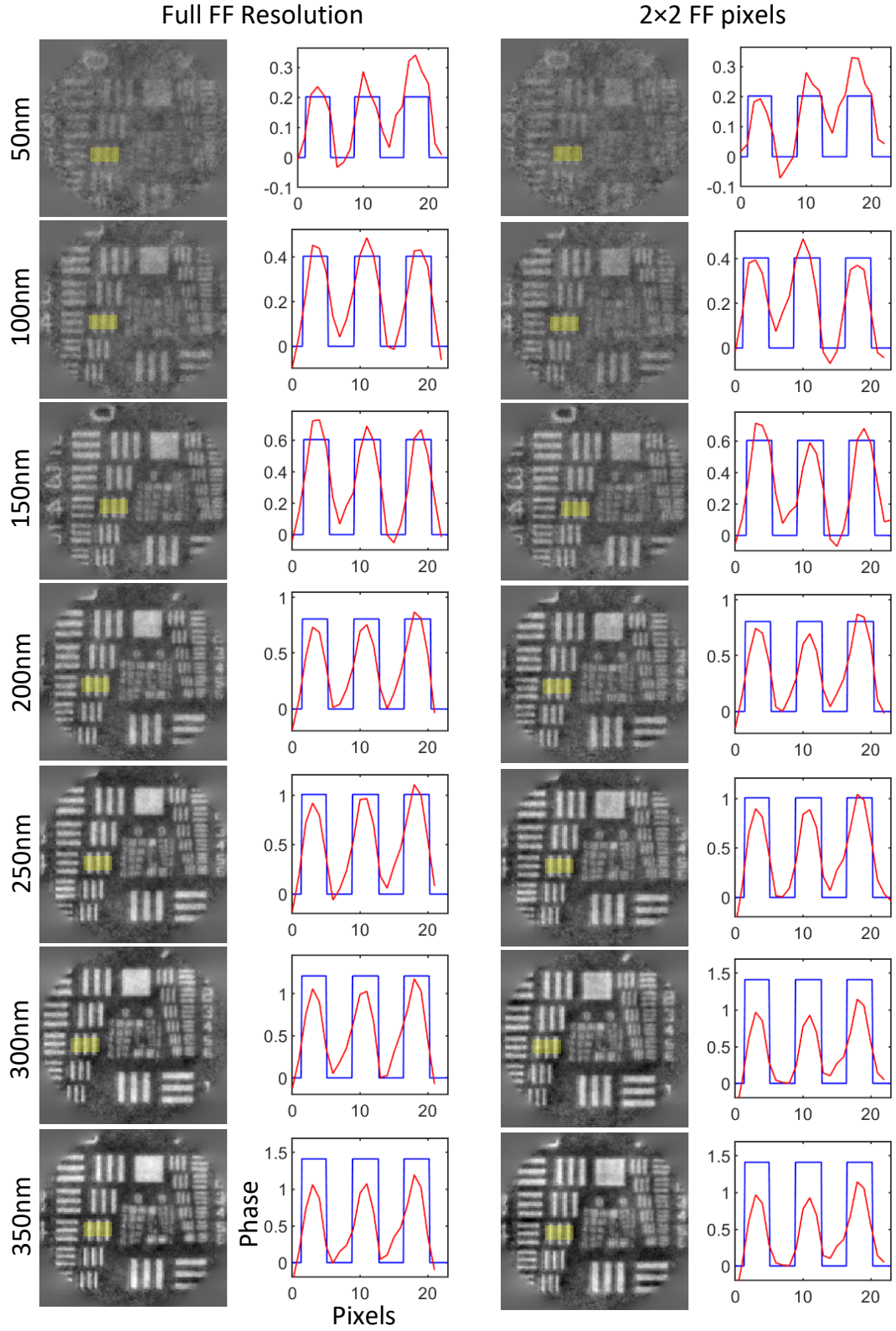


FIG. 9. Recovered phase image and cross-section of the highlighted region for all 1951 USAF resolution phase targets.

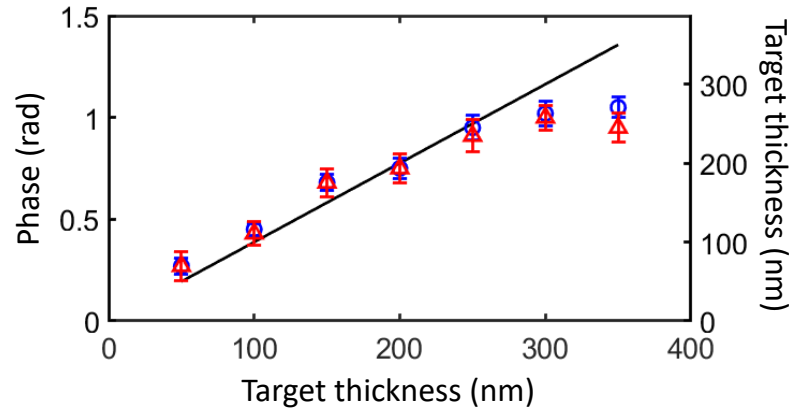


FIG. 10. Recovered phase as a function of the target thickness for the 1951 USAF target. Red triangles are the results for after a 30×30 binning is applied to the idler photons' position, whereas blue circles are when no binning is applied.

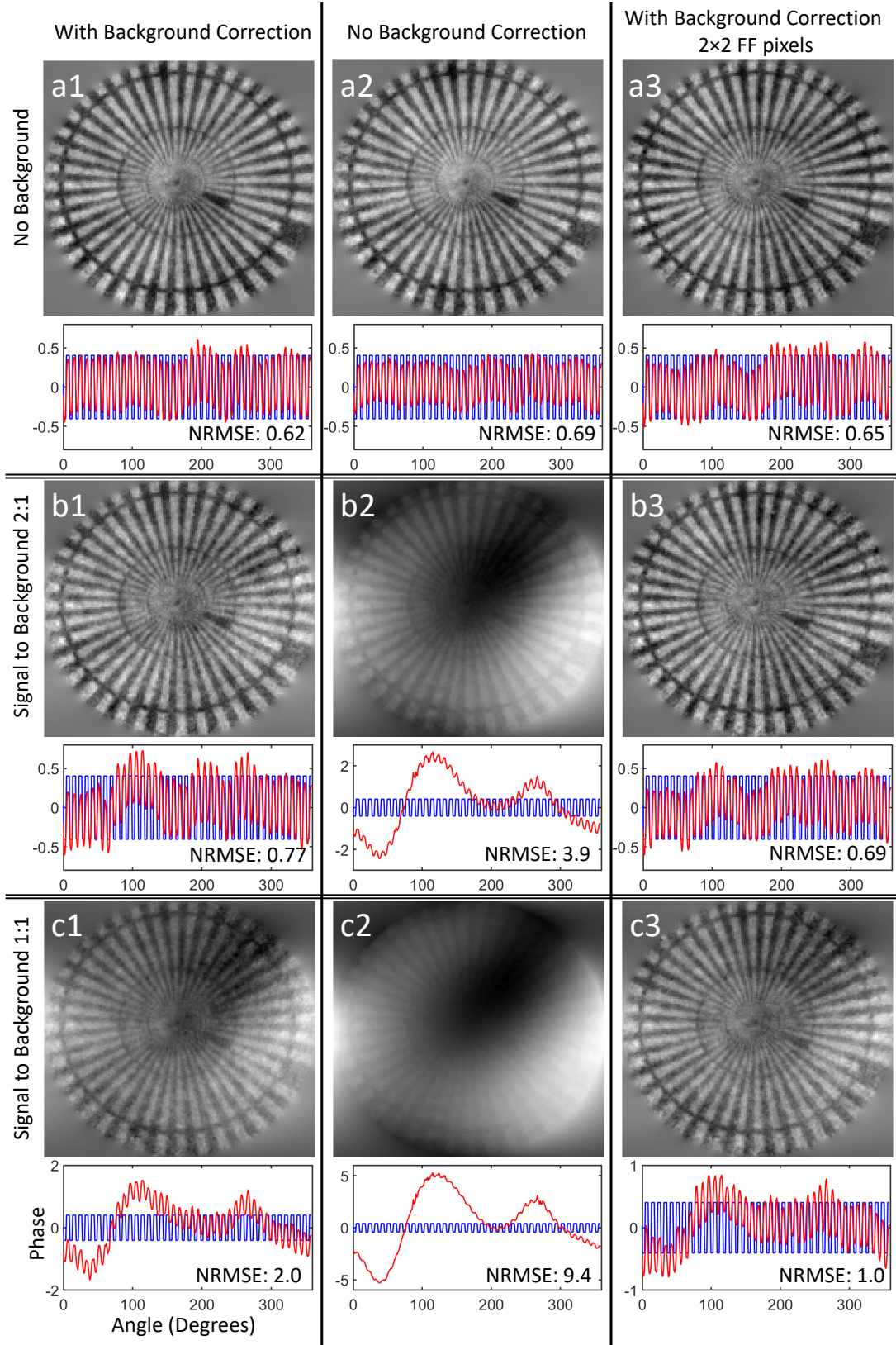


FIG. 11. Recovered phase image and cross-section of Star resolution phase targets to illustrate the background subtraction.